CuCo DAC used to change the hydrogenation sequence for efficient electrochemical C-N coupling

Zheng Lv, Liang Zhao, Shuanglong Zhou, Mengna Wang, Wenxia Xu, Jianping Lai [*], Lei Wang [*]

Key Laboratory of Eco-Chemical Engineering, Ministry of Education, International Science and Technology Cooperation Base of Eco-Chemical Engineering and Green Manufacturing, College of Chemistry and Molecular Engineering, Qingdao University of Science and Technology, Qingdao 266042, PR China

ARTICLE INFO

ABSTRACT

Cu-based diatomic catalysts have been reported to selectively synthesize urea. However, problems such as high applied potential (–0.6 ~ –1.5 V vs. RHE) and low urea yields are still being faced. In this article, we report a new class of CuCo diatomic catalyst (CuCo DAC) that exhibits high synthetic performance with a urea yield of 1.04 mol h^{-1} g$_{CuCo}^{-1}$ corresponding to a low applied potential (–0.45 V vs.RHE). This is the first reported molar level yield. In situ IR spectroscopy, TPD, H/D exchange experiment and DFT verified the effect of varying the hydrogenation sequence on urea properties. By optimizing the hydrogenation sequence of the reaction, an important nitrogen-containing intermediate (*NH$_2$) for NO$_3^-$ reduction is directly coupled with CO$_2$RR intermediates to achieve efficient urea electrosynthesis. The direct coupling of *NH$_2$ and *CO can effectively increase the chances of C-N coupling and lower the rate-determining step energy barrier.

1. Introduction

Urea is one of the important raw materials for basic chemicals and the most important nitrogen fertilizer for crop growth [1–4]. Currently, urea is industrially synthesized from ammonia and carbon dioxide at high temperatures and pressures [5–7]. This process requires high equipment requirements and requires a large amount of energy, which contributes to greenhouse gas emissions [8–10]. Therefore, it is worthwhile to develop a "green" and sustainable method of urea synthesis under environmental conditions to replace the traditional urea synthesis process [11–13]. To date, the direct activation of N$_2$ and CO$_2$ coupling for urea electrosynthesis under ambient conditions has remained extremely challenging due to the high-energy barriers required for the dissociation of the highly stable N≡N (941 kJ mol^{-1}) and C=O (806 kJ mol^{-1}) bonds as well as the side-reaction of ammonia generation [14–19]. In view of this, NO$_3^-$, which contains a reactive nitrogen-oxygen bonding component, is a more reactive nitrogen feedstock [20–22]. It can be obtained from industrial wastewater or through sustainable nitrate synthesis techniques. In addition, for the electrochemical synthesis of urea, the lower dissociation energy of the nitrogen-oxygen bond (204 kJ mol^{-1}) simplifies the coupling of NO$_3^-$ reduction to CO$_2$ reduction [23–25]. Therefore, NO$_3^-$ as a nitrogen source for urea synthesis is an ideal reactant to study electrochemical C-N bond formation [26–28].

Cu-based catalysts are widely used in C-N coupling reactions due to their low cost and high activity [29–32]. Dual-atom catalysts with maximized atom exposure can enhance catalytic performance [33] by creating synergistic effects between the two active sites. Edward H. Sargent and co-workers first reported a Zn/Cu hybrid diatomic catalyst that significantly improves the selectivity of urea synthesis through a relay catalytic mechanism [34]. However, currently reported Cu-based diatomic catalysts still face issues such as high application potential (–0.6 ~ –1.5 V vs. RHE) and low urea yield [35–37]. The reason is that they coupled *CO directly to large nitrogen-containing groups (*NO, *NO$_2$, etc.) to form a C-N bond first, and then deoxygenated and hydrogenated alternately on both sides of the coupling product, resulting in a rate-determining step with an excessively high energy barrier [38–41].

Based on the above considerations, by optimizing the hydrogenation sequence of the reaction intermediates, an important nitrogen-containing intermediate (*NH$_2$) for NO$_3^-$ reduction is directly coupled with CO$_2$ reduction intermediates may be a feasible way to achieve efficient urea electrosynthesis [42,43]. Previously reported Co SAC [44] can selectively reduce *NO intermediates to *NH$_2$ [45]. However, CuCo diatoms have not yet been used in C-N coupling reactions.

Here, we report a new class of CuCo DAC for efficient electrochemical C-N coupling reactions. Its urea yield rate can reach 1.04 mol h^{-1} g$_{CuCo}^{-1}$. This is the first reported molar level yield. The TOF

---

was 95.7 s^{-1}, significantly higher than the highest reported level (7.5 s^{-1}). After 10 cycles of testing, there was no significant change in urea yield. Finally, our systematic study of the reaction pathways and intermediates combined with in situ infrared spectroscopy, programmed temperature-raising adsorption (TPD), H/D exchange experiment and density-functional theory (DFT) calculations showed that changing the hydrogenation sequence is an effective strategy for achieving efficient electrosynthesis of urea. By changing the hydrogenation sequence, nitrate is continuously hydrogenated to generate *NH$_2$. This enables direct coupling between *NH$_2$ and *CO, reduces the reaction energy barrier of the rate determining step, and increases the probability of C-N coupling, all of which improve the electrosynthetic performance of urea [46–48].

2. Experimental section

2.1. Materials synthesis

2.1.1. Preparation of CuCo DAC

The synthesis of the materials was carried out using methods reported in the literature. 3.1 mg Co(Ac)$_2$•4H$_2$O, 2.5 mg Cu(Ac)$_2$•H$_2$O, 4 mg melamine, and 100 mg carbon blacks were dissolved in 15 mL ethanol. The mixture was alternately sonicated and stirred for five hours. Then, the resulting slurry was heated in an oil bath at 60℃ under continuous magnetic stirring until the solvent evaporated completely, yielding a black solid. The black solid obtained was ground with a mortar and pestle for 30 min, then transferred into a ceramic crucible and heated up in a tube furnace to 800℃ under a gas flow of 100 standard cubic centimeters per minute (sccm) Ar and maintained for 2 h, obtaining the final products. Inductively coupled plasma atomic emission spectroscopy (ICP-AES) analysis revealed that the content of Co and Cu was 0.64 wt% and 0.78 wt%.

2.1.2. Preparation of Cu SAC

The preparation of Cu SAC was essentially the same as that of CoCu DAC, except that Co(Ac)$_2$•4H$_2$O was missing from the reactants. ICP-AES analysis revealed that the content of Cu was 0.83 wt%.

2.1.3. Preparation of Co SAC

The preparation of Co SAC was essentially the same as that of CoCu DAC, except that Cu(Ac)$_2$•H$_2$O was missing from the reactants. ICP-AES analysis revealed that the content of Co was 0.71 wt%.

2.2. DFT calculation

All the spin-polarized DFT calculations are performed by the Vienna Ab initio Simulation Package (VASP) with the projector augmented wave (PAW) method. Graphene supercell with 62 carbon, 6 nitrogen, 1 Co and 1 Cu atoms was chosen to simulate catalyst. The exchange-functional is treated using the generalized gradient approximation (GGA) with Perdew-Burke-Ernzerhof (PBE) functional. The energy cut-off for the plane wave basis expansion was set to 520 eV. Partial occupancies of the Kohn−Sham orbitals were allowed using the Gaussian smearing method and a width of 0.05 eV. The vacuum spacing in a direction perpendicular to the plane of the structure is 15 Å for the surfaces. The Brillouin zone integration is performed using 2×2×1 Monkhorst-Pack k-point sampling for a structure. The self-consistent calculations apply a convergence energy threshold of 10^{-4} eV, and the force convergency was set to 0.05 eV/Å.

The reaction free energy was calculated following the computational hydrogen electrode (CHE) model.

The free energy corrections were considered at the temperature of 298 K, following:

$$\Delta G = \Delta E + \Delta G_{ZPE} + \Delta G_U - T\Delta S$$

where ΔE, ΔG$_{ZPE}$, ΔG$_U$, and ΔS refer to the DFT calculated energy change, the correction from zero-point energy, the correction from inner energy and the correction from entropy.

The free energy corrections were considered at the temperature of 298 K, following:

$$\Delta G = \Delta E + \Delta G_{ZPE} - T\Delta S$$

where ΔE, ΔG$_{ZPE}$, ΔGU, and ΔS refer to the DFT calculated energy change, the correction from zero-point energy and the correction from entropy.

3. Results and discussion

3.1. Synthesis and structural characterization of CuCo DAC

This material was prepared using a version of a previously published method [49–51]. The specific experimental steps can be found in the synthesis method section of the supporting information. Firstly, powder X-ray diffraction (XRD) was performed in order to analyze the phase composition of the prepared catalysts. As shown in Fig. S1, only two broad peaks at 24.2° and 43.8° were observed in all three samples, which can be attributed to (002) and (101) diffraction of graphitic carbon. The absence of any peaks forming metal crystals suggests that all metal atoms may be present in all samples in atomically dispersed form. In addition, the three samples were characterized by Raman spectroscopy and the results are shown in Fig. S2, in which graphite only has characteristic peaks at 1339 cm^{-1} and 1611 cm^{-1} and no other stray peaks were observed. Raman spectroscopy also confirmed that no crystalline phase was formed in the three samples. The powder XRD results are in agreement with the Raman spectroscopy results and provide preliminary evidence for possible atomic-level dispersion of metal atoms in the carbon blacks. However, due to the poor resolution of both characterizations, the presence of a small number of cluster structures still cannot be excluded. Therefore, subsequent characterization with higher precision is required.

In order to further analyze the microstructure of the catalyst, the catalyst was characterized by transmission electron microscopy (TEM). As can be seen from Fig. 1a and Fig. S3-S5, no metal nanoparticles were observed in any of the samples. However, the presence of clusters still cannot be ruled out as conventional TEM has only nanometre resolution. Therefore, an aberration-corrected high-angle annular dark field scanning transmission electron microscope (AC-HAADF-STEM) with a resolution up to Ångstrom level was used to further analyze the distribution of metal atoms on the substrate [52]. As shown in Fig. 1b, under dark-field conditions, only a large number of uniformly distributed bright white spots are observed on the substrate for the CuCo DAC. These bright spots can be assigned to cobalt and copper atoms because metal atoms have greater contrast in the dark field. No aggregation of metal atoms is observed at Ångstrom-level resolution, indicating that Co and Cu atoms are atomically dispersed on the substrate. In addition, many atom pairs were observed in Fig. 1b, suggesting that the formed Cu and Co atoms may appear in pairs on the substrate. The distance between the atomic pairs was measured to be about 0.24–0.25 nm. The energy dispersive spectroscopy (EDS) element mapping shows that Co, Cu, C, and N are uniformly distributed throughout the structure (Fig. 1c). Meanwhile, we performed the same EDS elemental mapping for Cu SAC and Co SAC and found that the various elements are uniformly distributed in the structure (Fig. S6-S7).

3.2. Characterization of coordination environment of CuCo DAC

In order to further accurately characterize the coordination environment of metal atoms, synchrotron radiation X-ray absorption spectroscopy (XAS) was conducted. Several standard Cu species (Cu foil, CuO, Cu$_2$O) and Co species (Co foil, CoO, Co$_2$O$_3$, Co$_3$O$_4$) were used as references. After pyrolysis, the k edge of Cu in CuCo DAC is lower than
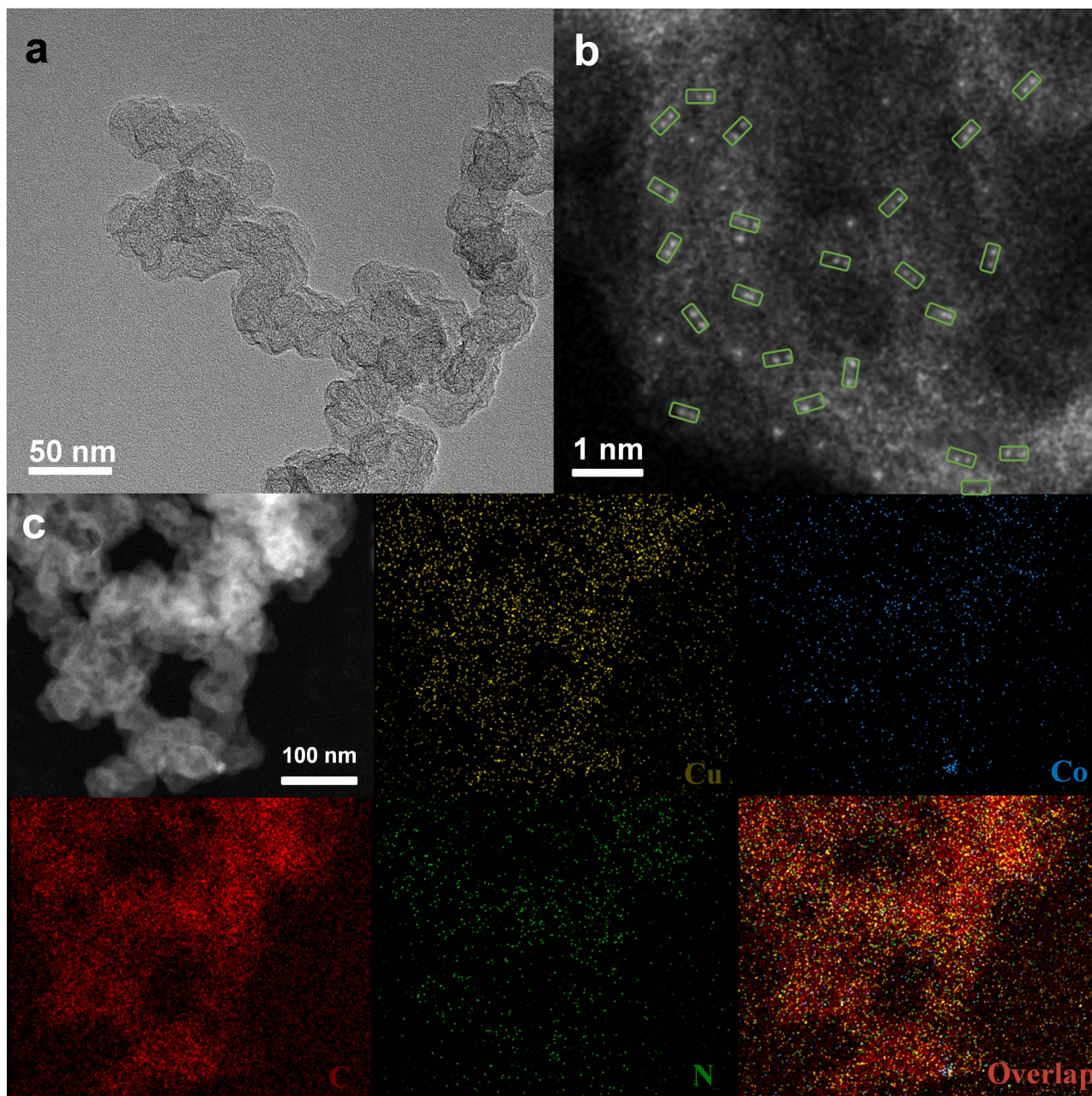
Fig. 1. (a) TEM and (b) HAADF-STEM image of CuCo DAC. (c) The corresponding element mapping of CuCo DAC.

that of Cu foil and Cu_2O, indicating that the valence state of Cu in CuCo DAC is close to +2 (Fig. 2a). In the FT-k^3 weighted EXAFS spectrum of CuCo DAC, there is a prominent peak at approximately 1.5 Å (Fig. 2b), similar to the peak positions of Cu_2O and CuO, rather than Cu. It is worth noting that no significant peak was observed in CuCo DAC around 2.24 Å, indicating that the number of Cu-Cu bonds can be ignored. The EXAFS results of Cu k edge are completely consistent with the simulated structure (Fig. 2c). The coordination number of Cu is about 3.8, and the average bond length is 1.944 Å (Table S1). Considering the influence of co coordination between C, O and Cu (such as O_2 or H_2O adsorbed when exposed to air), we can infer that the vast majority of Cu atoms in CuCo DAC are coordinated with four N atoms (Fig. 2c). The optimized Cu foil, CuO, and CuCoDAC fitting curves are shown in Fig. S8. Similarly, the near edge of the Co site in CuCo DAC is located between Co_2O_3 and Co_3O_4 (Fig. 2d), indicating that the valence state of Co is close to +2. The FT-k^3 weighted EXAFS spectrum of Co in CuCo DAC exhibits a main peak at 1.59 Å (Fig. 2e), indicating that the atomic coordination of Co is with

N. Meanwhile, the peak at 2.16 Å is weak, indicating that only trace Co-Co bonds have been formed in CuCo DAC. The EXAFS results of Co k edge are completely consistent with the simulated structure (Fig. 2f). The coordination number of Co is about 3.8, and the average bond length is 2.009 Å (Table S1). Considering that Co may adsorb O_2 or H_2O when exposed to air, we can infer that most of the Co atoms in CuCo DAC coordinate with four N atoms to form CoN_4 atomic sites. The fitting curves of the optimized Co foil, CoO, and CuCo DAC are shown in Fig. S9.

In addition, wavelet transform (WT) was performed to analyze the K-edge EXAFS oscillations of Cu (Fig. 2g) and Co (Fig. 2h). In Fig. 2g, the maximum WT value at 4.5 Å^{-1} is assigned to the Cu−N bond in CuN_4, which is consistent with the EXAFS results. Meanwhile, referring to the WT diagrams of Cu foil and CuO (Fig. S10a-b), the maximum strength value was not detected at 7 Å^{-1}, indicating that the number of Cu-Cu bonds can be ignored[53]. According to the WT plots of Co foil and CoO (Fig. S10c-d), the maximum strength value was not detected at
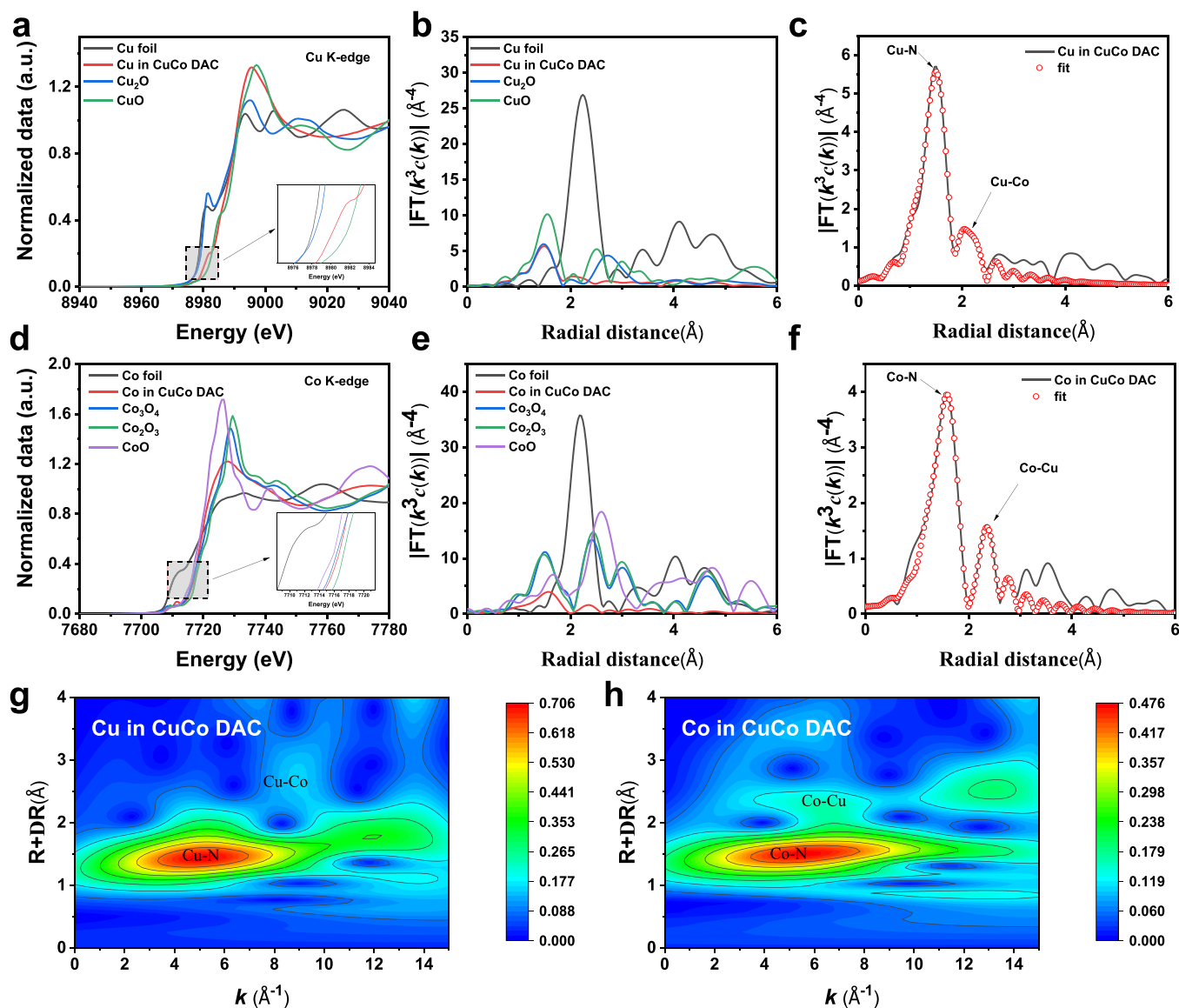
Fig. 2. (a) Normalized Cu k-edge XANES spectra of different samples. (b) Fourier transform EXAFS spectra of Cu related samples. (c) Corresponding Cu K-edge EXAFS fitting curves of CuCo DAC in R space. (d) Normalized Cu k-edge XANES spectra of different samples. (e) Fourier transform EXAFS spectra of Cu related samples. (f) Corresponding Co K-edge EXAFS fitting curves of CuCo DAC in R space. Wavelet transform of k^2-weighted EXAFS signal for Cu (g) and Co (h) in CuCo DAC.

7.8 Å^{-1}, indicating that the amount of Co-Co bonds was below the detection limit. It is worth noting that a sub center strength was detected in both Fig. 2g and h, which is attributed to the presence of Cu-Co bonds, consistent with the STEM results. Based on these results, we can conclude that the Cu and Co species in CuCo DAC coexist as diatomic sites, namely CuN$_4$ and CoN$_4$, anchored together on the carbon black.

Based on all the above characterization analyses, it can be determined that we have successfully synthesized a CuCo DAC. The Co/Cu metal atoms on the substrate are uniformly distributed at the atomic level, and a large number of Co-Cu atom pairs exist, with strong interactions formed between Co and Cu atoms. Detect the content of metal elements in the catalyst by inductively coupled plasma atomic emission spectroscopy (ICP-AES) (Table S2). The content of Co and Cu in CuCo DAC is 0.64 wt% and 0.78 wt%, respectively. The Co content in Co SAC is 0.71 wt%, and the Cu content in Cu SAC is 0.83 wt%. X-ray photoelectron spectroscopy (XPS) measurement to characterize the valence states of each atom. It was found that the weak peak intensity in the spectra of Cu 2p and Co 2p (Fig. S11) is related to the high dispersion and low content of Cu (0.78 wt%) and Co (0.64 wt%). This corresponds

to the ICP-AES results.

3.3. The electrocatalytic performance of CuCo DAC and its comparison samples

The synthesized CuCo DAC and control samples were tested for urea electrosynthesis reaction under the same conditions. Firstly, their electrochemical performance was tested in a commonly used H-type electrolyze system. The cathode and anode were separated by a Nafion 117 membrane to prevent the products of cathodic reduction from being oxidized by the anode, and CO$_2$ gas was continuously pumped into the cathodic electrolyte (0.1 M KHCO$_3$ + 0.1 M KNO$_3$). The reaction was carried out with CO$_2$ as the carbon source and KNO$_3$ as the nitrogen source, and the CO$_2$ was aerated for at least 30 min before the reaction, and all electrochemical tests were carried out on a CHI 760 workstation. In addition, all potentials mentioned in this paper are related to the reversible hydrogen electrode (RHE).

Firstly, the potential performance of CuCo DAC for electrocatalytic coupling of CO$_2$ and NO$_3^-$ reduction to produce urea was evaluated using

linear scanning voltammetry (LSV). As shown in Fig. 3a, the current density of the CuCo DAC was higher than that of the monometallic Co SAC and significantly higher than that of the monometallic Cu SAC in a mixed solution of 0.1 M $KHCO_3$ + 0.1 M KNO_3 with continuous injection of CO_2 gas, indicating that the introduction of the bimetallic metal has a better ability to activate CO_2 and NO_3, and that the CuCo DAC has a better onset potential. The electrosynthesis activity of urea was tested in the range around the starting potential. The curves of current density versus time recorded at different potentials illustrated the stability of the CuCo DAC (Fig. S12), and in addition, continuous stability tests up to 100 h were carried out (Fig. S13), where smooth current density curves illustrated the superior stability of the catalyst. In order to exclude catalyst reconfiguration during the reaction process, we performed spherical aberration electron microscopy tests on the reacted material. The diatomic phase was found to be stable and not destroyed (Fig.S14). In addition, we tested the electrolyte after a long period of electrolysis and found that there was almost no leaching of metal ions from the electrolyte, which implies that CuCo DAC has excellent electrochemical stability. The urea synthesis performance was tested near the starting potential, and the generated urea was quantified using diacetylmonoxime and ^1H NMR methods. The calibration curves are shown in Fig. S15. Notably, the generated hydroxylamine was also calibrated due to the selective synthesis of hydroxylamine in the reaction. The calculated urea yields and Faraday efficiencies in Fig. 3b show that the CuCo DAC at −0.45 V vs. RHE gave the highest urea yield of 1.04 mol h^{-1} g^{-1}_{CuCo}. This is the first reported molar level yield (Table S3), with a Faraday efficiency of 45.85%. And the Faraday efficiency of hydroxylamine, a by-product, reached 43.56%. In addition to exploring the effect of different voltages on the selectivity of urea synthesis, we also explored the effect of different pH ranges on the selectivity of urea synthesis

(Fig. S16). The results showed that both acid and alkali were unfavorable for the synthesis of urea. This catalyst has the highest performance in urea synthesis in neutral solutions. In addition, we provide the performance of the catalysts in terms of conversion rate, overpotentials, partial current density, selectivity, etc. (Table S4). Similarly, we also tested the effect of catalysts with different CuCo contents on the urea synthesis performance (Fig. S17). The results indicate that when one element content remains constant and the other element content increases, the urea performance slightly decreases. However, due to the increase in element content, it is inevitable to bring about problems such as atomic particle aggregation and obstruction of active sites. When the content of one element remains unchanged and the content of another element decreases, the urea synthesis performance decreases significantly, which may be due to insufficient active sites. The UV curves of urea synthesis performance at different potentials are shown in Fig. S18a. After ten cycles of experiments, the yield of urea was maintained at 1.00 mol h^{-1} g^{-1}_{CuCo}, and the Faraday efficiency was at 44.04% (Fig. 3c and Fig. S18b). The concentration of urea obtained from the ^1H NMR peak area integral calculation was in general agreement with the UV detected concentration. We then collected the different product distributions during the reaction by gas chromatography (shown in Fig. 3d) and found that small amounts of CO, H_2 and NO_2^- were generated during the reaction in addition to urea and hydroxylamine. The presence of N_2 and NO was not detected. The concentration of nitrite at different potentials is shown in Fig. S19. We also compared the product Faraday efficiency distributions of Cu SAC and Co SAC (Fig. S20-S21) and found that the Faraday efficiency of hydroxylamine on Co SAC was higher than that on CuCo DAC, probably due to the fact that more hydroxylamine produced by CuCo DAC was used for the synthesis of urea. It is noteworthy that very small amounts of NH_3 were produced on the
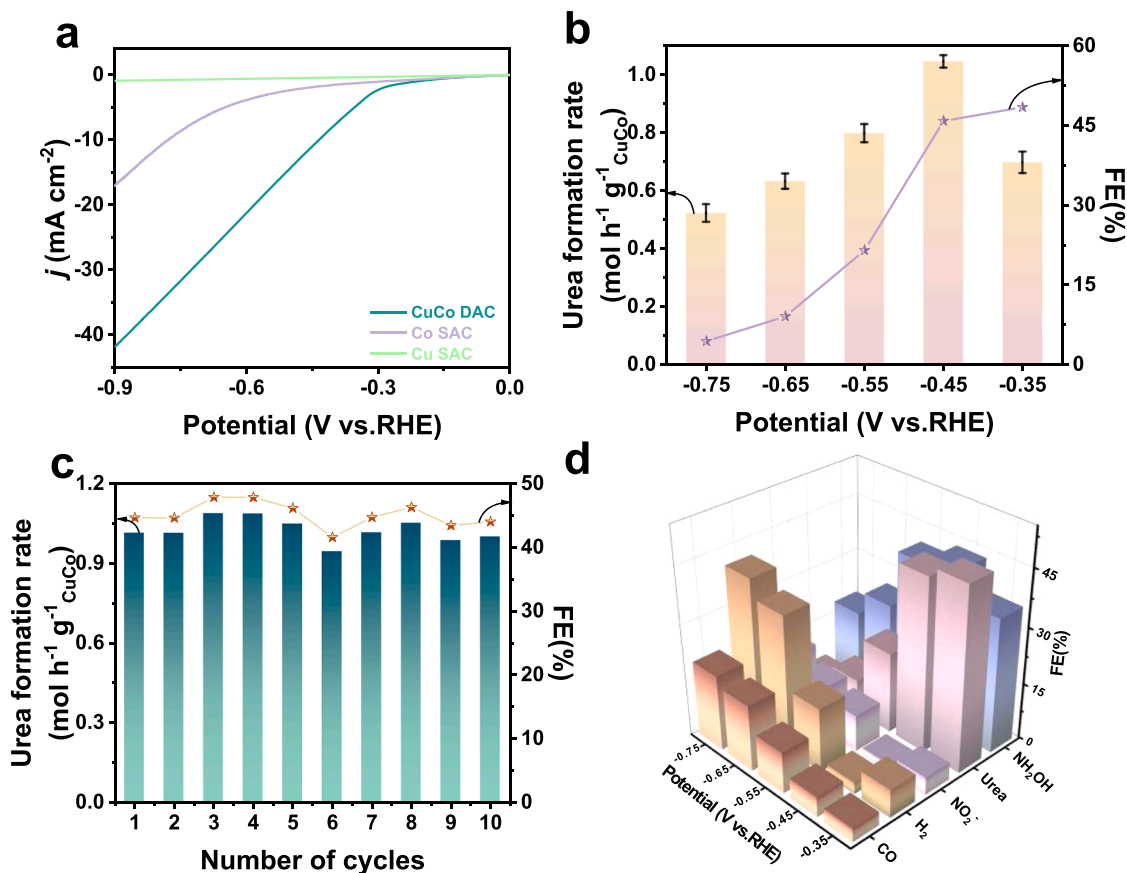

Fig. 3. (a) Comparison of LSV of CuCo DAC, Co SAC, and Cu SAC in CO_2 saturated electrolytes. (b) Urea yield and Faraday efficiency of CuCo DAC at different potentials. (c) The Faradaic efficiency and urea production rate of CuCo DAC catalyst at −0.45 V vs. RHE during recycling tests ten times. (d) The product Faraday efficiency distribution of catalysts using NO_3 and CO_2 as raw materials at different potentials.

CuCo DAC during urea synthesis, which is inconsistent with our inferred pathway. In order to investigate the origin of these small amounts of NH_3, we introduced an appropriate amount of formaldehyde into the electrolyte to capture the produced NH_2OH in situ, and after the introduction of formaldehyde, no ammonia was detected again in the reaction system, which implies that the small amount of ammonia was produced by the decomposition/conversion of NH_2OH. Moreover, only NH_3 was detected as a by-product of NO_3^- reduction on Cu SAC, further suggesting that the selective generation of hydroxylamine is related to the Co site this will be further explained in the DFT calculations.

3.4. In situ characterization and isotope testing of catalysts

To explain the better urea synthesis performance of CuCo DAC, we performed CO_2-TPD tests on the three materials (Fig. 4a) and found the relative strength of the adsorption peaks of Co SAC and Cu SAC is very weak, indicating that a single Cu SAC and Co SAC has poor adsorption capacity for CO_2. CuCo DAC has a higher and stronger adsorption strength, indicating its strong adsorption ability for CO_2. It is worth noting that the CO_2-TPD of CuCo DAC exhibits a bimodal pattern, further proving that the prepared CuCo atoms did not form an alloy but were distributed separately in the catalytic system. Strong CO_2 adsorption can timely replenish the CO_3^{2-} concentration in the solution, which is beneficial for the enrichment of reactants. Subsequently, the involvement of intermediates generated during urea synthesis was further

investigated by in situ infrared spectroscopy. The peak at 3614 cm^{-1} in Fig. 4b, c is the stretching vibration peak of the N-H bond, while the adsorption peak of the CO_2 molecule should be located at 3552 cm^{-1} [48]. The peak at 3145 cm^{-1} should be attributed to NH_2 [54]. The peak at 1623 cm^{-1} is attributed to the bending vibration of adsorbed water. Also, the peaks at 1537 cm^{-1} should be attributed to the bending vibrations of the N-H bond in NH_2OH [11]. The peak at 1112 cm^{-1} should be attributed to the C-O stretching vibration [54]. Respectively, the peak at 1259 cm^{-1} is NH_2 stretching vibration peak [40], and the peak at 2112 cm^{-1} is attributed to *$CONH_2$. More importantly, a typical peak at 1449 cm^{-1} was observed at all given potentials, indicating the successful formation of the C-N bond in the *$CONH_2$ intermediate [20]. The enhancement of the peak strength of the C-N bond at -0.45 V vs. RHE potential is also consistent with our experimental results. In addition, we also conducted in situ infrared testing on individual Cu SAC and Co SAC, and the results are shown in Fig. S22. During the Cu test, only the relevant C=O stretching vibration peak was observed, and no NO_3RR related product peak was observed, indicating that the CO_2RR reaction was carried out at the Cu site. Similarly, during Co SAC testing, peaks related to NO_3RR reduction were observed, while the absence of a CO_2RR product peak indicates that the Co site undergoes nitrate reduction reaction. The presence of these key intermediates provides the existence of a new pathway for urea synthesis. In order to eliminate false-positive results in the experiments, we performed a series of control experiments and demonstrated by isotope experiments (Fig. 4d) that
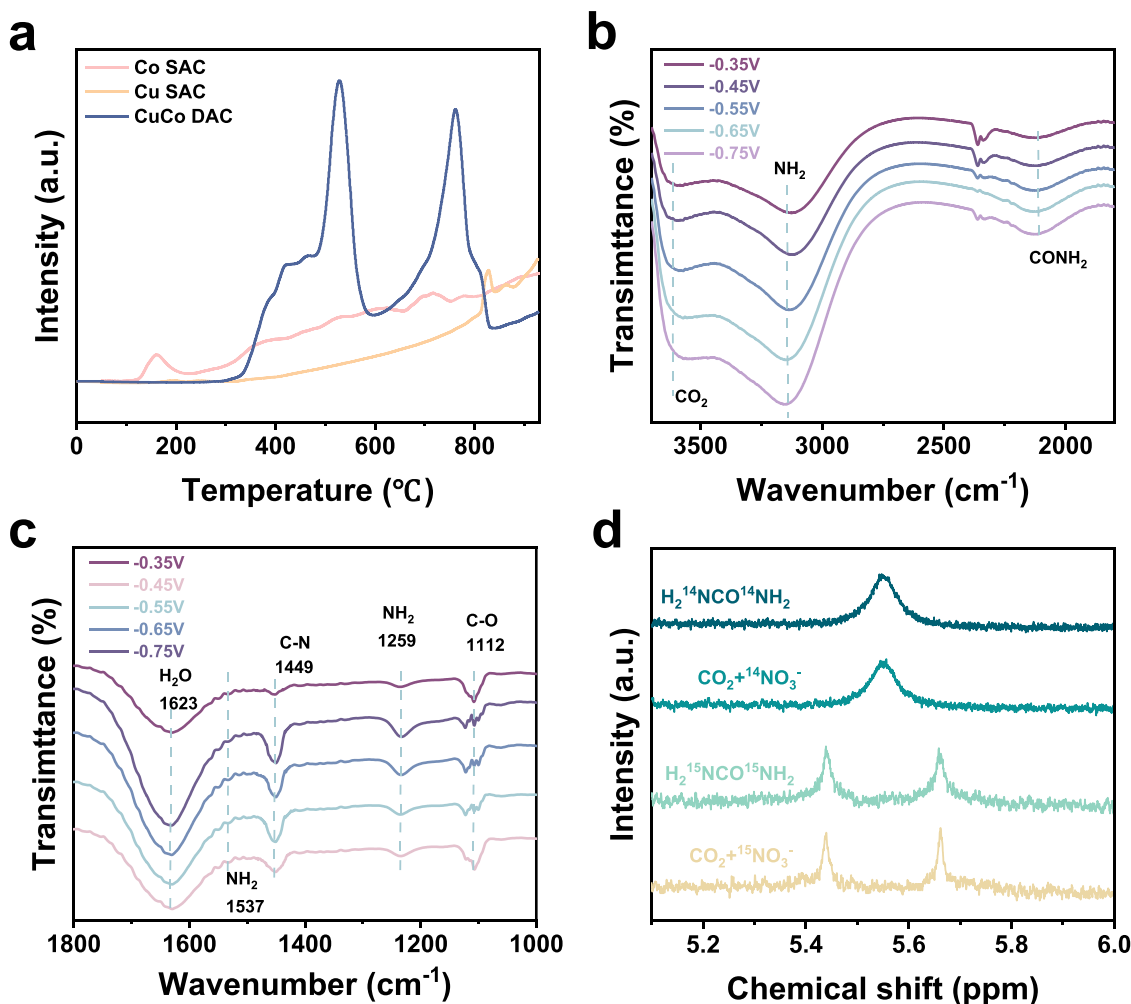

Fig. 4. (a) Carbon dioxide temperature-programmed desorption (CO_2-TPD) spectra of CuCo DAC. (b) Infrared signal in the range of (c)1800–3600 cm^{-1} and (c) 1000–1800 cm^{-1} under various potentials for CuCo DAC during the electrocoupling of NO_3^- and CO_2. (d) ^1H NMR spectra of electrolyte saturated with $^{15}NO_3^-$ + CO_2/$^{14}NO_3^-$ + CO_2 after 1 h electrolysis and standard $^{15}NH_2CO^{15}NH_2$/$^{14}NH_2CO^{14}NH_2$ solution.

the generated urea was derived from NO_3^- in solution and CO_2 injected at the same time, and not from pollutants. When $^{15}NO_3^-$ and CO_2 were used as feed gases, no significant $CO(NH_2)_2$ signals were observed, and only $CO(^{15}NH_2)_2$ signals were detected in the reacting electrolyte, confirming the generation of urea from the simultaneous reduction of NO_3^- and CO_2. This result strongly excludes false-positive results from the experiment (Fig. S23). To further illustrate the effect of changing the hydrogenation sequence on urea electro synthesis, we conducted H/D exchange experiments for testing. Research has found that when H in the solution is completely replaced by D, the performance of urea synthesis significantly decreases (Fig. S24), indicating a close correlation between urea synthesis and the formation of H-containing intermediates. The activity of D atoms decreases, and the yield of urea also decreases relatively.

To reveal the role of diatomic sites in urea synthesis, we also investigated the electrochemical properties of CuCo DAC with Cu SAC and Co SAC. In Fig. S25, CuCo DAC exhibits a larger electrochemically active surface area (ECSA) and can provide a larger number of active sites, providing a theoretical basis for urea synthesis. Compared with Cu SAC and Co SAC, CuCo DAC has a smaller impedance (Fig. S26) and larger ECSA (Fig. S25). This echoes the results of the CO_2-TPD test. In addition, we performed conversion frequency tests in 1 M phosphate buffer solution (pH = 7.4) and were able to achieve a TOF value of 93.73 s^{-1} at a current density of 10 mA cm^{-2} (Fig. S27), significantly higher than the highest reported level (7.5 s^{-1}) [15].

3.5. DFT calculation of C-N coupling in neutral media

DFT calculations strongly confirm the role of diatomic catalysts in urea synthesis. As expected, the linear adsorption of the *NO

intermediate at the Co site maintained the N-O bond and continued hydrogenation at the N site to produce *NH_2O instead of *NOH or *NHOH (Fig. 5a). After determining the hydrogenation sequence of the *NO intermediate, we analyzed the complete NO_3^- reduction process (Fig. 5b). Due to the change in hydrogenation sequence, hydroxylamine can be generated, and the presence of hydroxylamine provides a new pathway for urea synthesis. The carbon dioxide reduction pathway diagram is shown in Fig. S28. All model structures are shown in Fig. S29-S34. We have analyzed and calculated the coupling between various nitrogen-containing intermediates and carbon dioxide reduction intermediates generated during the nitric acid reduction process. As previously reported, the coupling between *NO_2, *NO or *NHO and *CO is a process of increasing free energy with high coupling energy barriers. However, changing the hydrogenation sequence to directly coupled between *NH or *NH_2 and *CO is a process of decreasing free energy that is easier to occur (Fig. 5c, d). However, due to the difficulty in generating *NH in the reaction, direct coupling between *CO and *NH_2 is the most suitable path. Similarly, the second step of coupling remains the same. The direct coupling of *CO with *NH_2 not only has small spatial site resistance but also avoids the subsequent deoxidation and hydrogenation processes of the coupling product. Combining TPD analysis and theoretical calculations, the CuCo DAC effectively increase the adsorption of inert gases on the catalyst surface while enhancing the formation and stability of key intermediates on the catalyst surface. By changing the hydrogenation sequence, the rate-determining step of C-N coupling was reduced, and the probability of C-N coupling was increased.
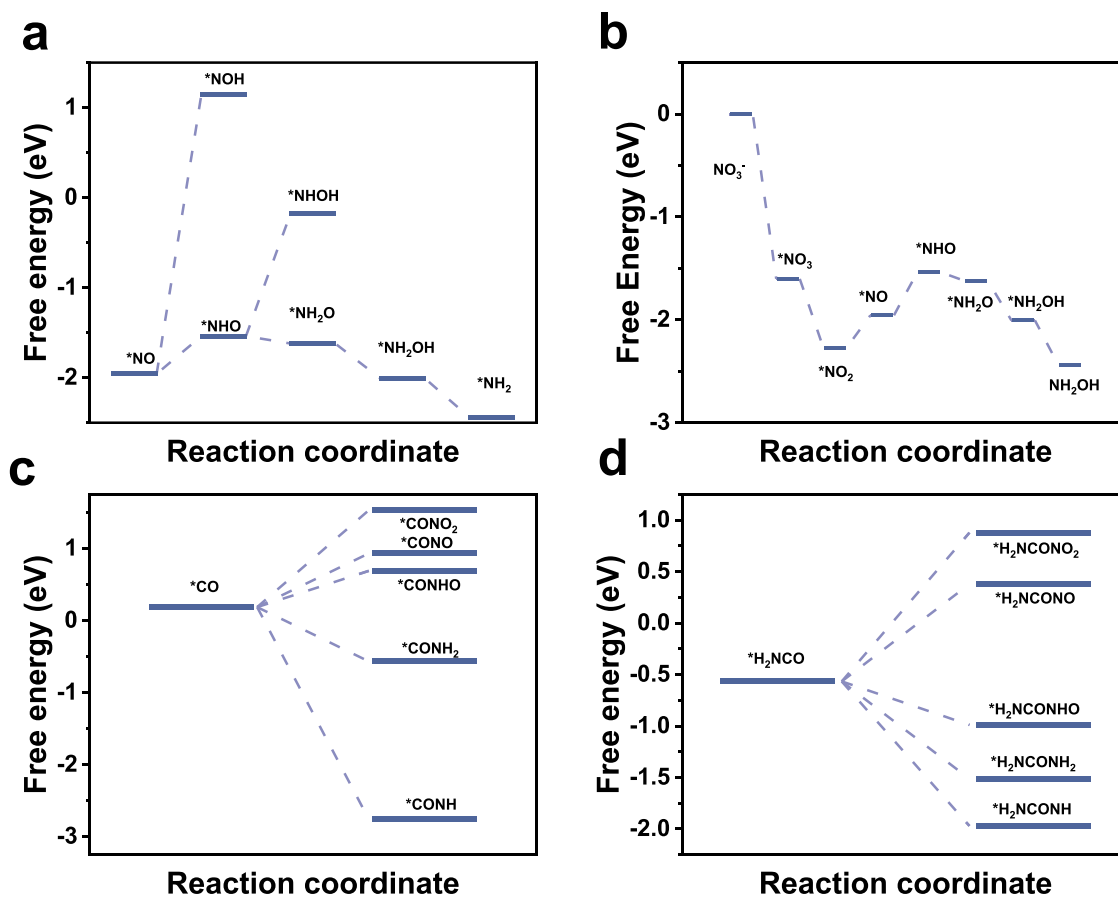

Fig. 5. (a) The free energy diagram of *NO changing the hydrogenation sequence. (b) Free energy diagram of nitrate reduction to hydroxylamine. (c) Comparison of the first coupling free energy between nitrogen-containing intermediates and *CO. (d) Comparison of the second coupling free energy between nitrogen-containing intermediates and *CO.

4. Conclusion

In summary, by changing the hydrogenation sequence of the nitrate reduction process, the reaction intermediates *NH_2 and *CO are directly coupled and the reaction energy barrier of the rate determining step is reduced. The urea yield rate of CuCo DAC can reach 1.04 mol h^{-1} g$^{-1}_{CuCo}$, which is the first reported molar level yield. In situ IR spectroscopy, TPD, H/D exchange experiment and DFT verified the effect of varying the hydrogenation sequence on urea properties. By optimizing the hydrogenation sequence of the reaction, an important nitrogen-containing intermediate (*NH_2) for NO_3^- reduction is directly coupled with CO_2-reducing intermediates to achieve efficient urea electrosynthesis. The direct coupling of *NH_2 and *CO can effectively increase the chances of C-N coupling and lower the rate-determining step energy barrier. This work emphasizes the practicality of catalysts that can change the hydrogenation sequence to achieve efficient C-N coupling reactions.

CRediT authorship contribution statement

Lei Wang and Jianping Lai supervised the research. Jianping Lai conceived the research. Jianping Lai and Zheng Lv designed the experiments and discussed the results. Zheng Lv. performed most of the experiments and wrote the manuscript. Liang Zhao helped with electrochemical measurements. Shuanglong Zhou helped answer some questions. Mengna Wang and Wenxia Xu helped with some formatting adjustments.

Declaration of Competing Interest

The authors declare that they have no known competing financial interests or personal relationships that could have appeared to influence the work reported in this paper.

Data availability

The authors do not have permission to share data.

Acknowledgements

Appendix A. Supporting information

Supplementary data associated with this article can be found in the online version at doi:10.1016/j.apcatb.2024.124003.

References

[1] M. Jouny, J. Lv, T. Cheng, B.H. Ko, J. Zhu, W. Goddard, F. Jiao, Formation of carbon–nitrogen bonds in carbon monoxide electrolysis, Nat. Chem. 11 (2019) 846–851, https://doi.org/10.1038/s41557-019-0312-z.

[2] Y. Liu, X. Tu, X. Wei, D. Wang, X. Zhang, W. Chen, C. Chen, S. Wang, C-bound or O-bound surface: which one boosts electrocatalytic urea synthesis? Angew. Chem. Int. Ed. 62 (2023) e202300387 https://doi.org/10.1002/anie.202300387.

[3] M. Yuan, J. Chen, Y. Xu, R. Liu, T. Zhao, J. Zhang, Z. Ren, Z. Liu, C. Streb, H. He, C. Yang, S. Zhang, G. Zhang, Highly selective electroreduction N₂ and CO₂ to urea over artificial frustrated lewis pairs, Energ. Environ. Sci. 14 (2021) 6605–6615, https://doi.org/10.1039/D1EE02485J.

[4] M. Yuan, J. Chen, H. Zhang, Q. Li, L. Zhou, C. Yang, R. Liu, Z. Liu, S. Zhang, G. Zhang, Host–guest molecular interaction promoted urea electrosynthesis over a precisely designed conductive metal–organic ramework, Energy Environ. Sci. 15 (2022) 2084–2095, https://doi.org/10.1039/D1EE03918K.

[5] Y. Zhou, A.J. Martín, F. Dattila, S. Xi, N. López, P.-R. Javier, B.S. Yeo, Long-chain hydrocarbons by CO₂ electroreduction using polarized nickel catalysts, Nat. Catal. 5 (2022) 545–554, https://doi.org/10.1038/s41929-022-00803-5.

[6] R. Wu, F. Li, X. Cui, Z. Li, C. Ma, H. Jiang, L. Zhang, Y. Zhang, T. Zhao, Y. Zhang, Y. Li, H. Chen, Z. Zhu, Enzymatic electrosynthesis of glycine from CO₂ and NH₃, Angew. Chem. Int. Ed. 62 (2023) e202218387, https://doi.org/10.1002/anie.202218387.

[7] Q. Zhao, X. Lu, Y. Wang, S. Zhu, Y. Liu, F. Xiao, S. Dou, W. Lai, M. Shao, Sustainable and high-rate electrosynthesis of nitrogen fertilizer, Angew. Chem. Int. Ed. 62 (2023) e202307123, https://doi.org/10.1002/anie.202307123.

[8] H. Zhang, Z. Zhou, Y. Yin, H. Xu, Y. Wang, K. Wang, Z. Zhang, J. Wang, X. He, Efficient capture and separation of CO₂-boosted carbon neutralization enabled by tailorable metal-organic frameworks: a review, EcoEnergy 1 (2023) 120148, https://doi.org/10.1002/ece2.15.

[9] P.M. Krzywda, A. Paradelo Rodríguez, N.E. Benes, B.T. Mei, G. Mul, Carbon-nitrogen bond formation on Cu electrodes during CO₂ reduction in NO₃⁻ solution, Appl. Catal. B Environ. 316 (2022) 121512, https://doi.org/10.1016/j.apcatb.2022.121512.

[10] J. Yuan, L. Hu, J. Huang, Y. Chen, S. Qiao, H. Xie, Photo/electrochemical urea synthesis via CO₂ coupling with nitrogenous small molecules: status and challenges for the development of mechanism and catalysts, Appl. Catal. B Environ. 339 (2023) 123146, https://doi.org/10.1016/j.apcatb.2023.123146.

[11] L. Pan, J. Wang, F. Lu, Q. Liu, Y. Gao, Y. Wang, J. Jiang, S. Chao, J. Wang, X. Wang, Single-atom or dual-atom in TiO₂ nanosheet: which is the better choice for electrocatalytic urea synthesis? Angew. Chem. Int. Ed. 62 (2022) e202216835 https://doi.org/10.1002/anie.202216835.

[12] A. Martín, F. Veenstra, J. Lüthi, R. Verel, J. Pérez Ramírez, Toward reliable and accurate ammonia quantification in the electrocatalytic reduction of nitrogen, Chem. Catal. 1 (2021) 1505–1518, https://doi.org/10.1016/j.checat.2021.10.002.

[13] Y. Jiao, H. Li, Y. Jiao, S. Qiao, Activity and selectivity roadmap for C-N electro-coupling on MXenes, J. Am. Chem. Soc. 145 (2023) 15572–15580, https://doi.org/10.1021/jacs.3c05171.

[14] D. Li, Y. Zhao, Y. Miao, C. Zhou, L. Zhang, L. Wu, T. Zhang, Accelerating electron-transfer dynamics by TiO₂ -immobilized reversible single-atom copper for enhanced artificial photosynthesis of urea, Adv. Mater. 34 (2022) e2207793, https://doi.org/10.1002/adma.202207793.

[15] Z. Lv, S. Zhou, L. Zhao, Z. Liu, J. Liu, W. Xu, L. Wang, J. Lai, Coactivation of multiphase reactants for the electrosynthesis of urea, Adv. Energ. Mater. 13 (2023) 2300946, https://doi.org/10.1002/aenm.202300946.

[16] C. Chen, X. Zhu, X. Wen, Y. Zhou, L. Zhou, H. Li, L. Tao, Q. Li, S. Du, T. Liu, D. Yan, C. Xie, Y. Zou, Y. Wang, R. Chen, J. Huo, Y. Li, J. Cheng, H. Su, X. Zhao, W. Cheng, Q. Liu, H. Lin, J. Luo, J. Chen, M. Dong, K. Cheng, C. Li, S. Wang, Coupling N₂ and CO₂ in H₂O to synthesize urea under ambient conditions, Nat. Chem. 12 (2020) 717–724, https://doi.org/10.1038/s41557-020-0481-9.

[17] X. Zhang, X. Zhu, S. Bo, C. Chen, K. Cheng, J. Zheng, S. Li, X. Tu, W. Chen, C. Xie, X. Wei, D. Wang, Y. Liu, P. Chen, S. Jiang, Y. Li, Q. Liu, C. Li, S. Wang, Electrocatalytic urea synthesis with 63.5% faradaic efficiency and 100% N-selectivity via one-step C-N coupling, Angew. Chem. Int. Ed. 62 (2023) e202305447, https://doi.org/10.1002/anie.202305447.

[18] S. Choe, N. Kim, Y.J. Jang, Perspective on the interfacial engineering for electrocatalytic N₂ to NH₃ conversion from catalysts to systems, EcoEnergy 1 (2023) 3–15, https://doi.org/10.1002/ece2.10.

[19] Y. Sun, Z. Sun, W. Zhang, W. Li, C. Liu, Q. Zhao, Z. Huang, H. Li, J. Wang, T. Ma, Fabricating freestanding electrocatalyst with bismuth-iron dual active sites for efficient ammonia synthesis in neutral media, EcoEnergy 1 (2023) 186–196, https://doi.org/10.1002/ece2.3.

[20] J. Geng, S. Ji, M. Jin, C. Zhang, M. Xu, G. Wang, C. Liang, H. Zhang, Ambient electrosynthesis of urea with nitrate and carbon dioxide over iron-based dual-sites, Angew. Chem. Int. Ed. 62 (2022) e202210958, https://doi.org/10.1002/adma.202300020.

[21] C. Chen, S. Li, X. Zhu, S. Bo, K. Cheng, N. He, M. Qiu, C. Xie, D. Song, Y. Liu, W. Chen, Y. Li, Q. Liu, C. Li, S. Wang, Balancing sub-reaction activity to boost electrocatalytic urea synthesis using a metal-free electrocatalyst, Carbon Energy (2023), https://doi.org/10.1002/cey2.345.

[22] X. Zhang, X. Zhu, S. Bo, C. Chen, M. Qiu, X. Wei, N. He, C. Xie, W. Chen, J. Zheng, P. Chen, S. Jiang, Y. Li, Q. Liu, S. Wang, Identifying and tailoring C–N coupling site for efficient urea synthesis over diatomic Fe–Ni catalyst, Nat. Commun. 13 (2022) 5337, https://doi.org/10.1038/s41467-022-33066-6.

[23] N. Meng, X. Ma, C. Wang, Y. Wang, R. Yang, J. Shao, Y. Huang, Y. Xu, B. Zhang, Y. Yu, Oxide-derived core-shell Cu@Zn nanowires for urea electrosynthesis from carbon dioxide and nitrate in water, ACS Nano 16 (2022) 9095–9104, https://doi.org/10.1021/acsnano.2c01177.

[24] J. Leverett, T. Tran-Phu, J.A. Yuwono, P. Kumar, C. Kim, Q. Zhai, C. Han, J. Qu, J. Cairney, A.N. Simonov, R.K. Hocking, L. Dai, R. Daiyan, R. Amal, Tuning the coordination structure of Cu-N-C single atom catalysts for simultaneous electrochemical reduction of CO₂ and NO₃⁻ to urea, Adv. Energy Mater. 12 (2022) 2201500, https://doi.org/10.1002/aenm.202201500.

[25] Q. Wu, C. Dai, F. Meng, Y. Jiao, Z.J. Xu, Potential and electric double-layer effect in electrocatalytic urea synthesis, Nat. Commun. 15 (2024), https://doi.org/10.1038/s41467-024-45522-6.

[26] Y. Feng, H. Yang, Y. Zhang, X. Huang, L. Li, T. Cheng, Q. Shao, Te-doped Pd nanocrystal for electrochemical urea production by efficiently coupling carbon

dioxide reduction with nitrite reduction, Nano Lett. 20 (2020) 8282–8289, https://doi.org/10.1021/acs.nanolett.0c03400.

[27] X. Liu, Y. Jiao, Y. Zheng, M. Jaroniec, S. Qiao, Mechanism of C-N bonds formation in electrocatalytic urea production revealed by ab initio molecular dynamics simulation, Nat. Commun. 13 (2022) 5471, https://doi.org/10.1038/s41467-022-33258-0.

[28] W. He, J. Zhang, S. Dieckhofer, S. Varhade, A. Brix, A. Lielpetere, S. Seisel, J. Junqueira, W. Schuhmann, Splicing the active phases of copper/cobalt-based catalysts achieves high-rate tandem electroreduction of nitrate to ammonia, Nat. Commun. 13 (2022) 1129, https://doi.org/10.1038/s41467-022-28728-4.

[29] Y. Guo, S. Huang, Y. Guo, Z. Ye, J. Nan, Q. Zhou, Y. Zhu, Efficient degradation of organic pollutants by enhanced interfacial internal electric field induced via various crystallinity carbon nitride homojunction, Appl. Catal. B Environ. 312 (2022) 121388, https://doi.org/10.1016/j.apcatb.2022.121388.

[30] S.-Q. Liu, M.-R. Gao, S. Liu, J.-L. Luo, Hierarchically assembling cobalt/nickel carbonate hydroxide on copper nitride nanowires for highly efficient water splitting, Appl. Catal. B Environ. 292 (2021) 120148, https://doi.org/10.1016/j.apcatb.2021.120148.

[31] Y. Pan, H. Li, J. Xiong, Y. Yu, H. Du, S. Li, Z. Wu, S. Li, J. Lai, L. Wang, Protecting the state of Cu clusters and nanoconfinement engineering over hollow mesoporous carbon spheres for electrocatalytical C-C coupling, Appl. Catal. B Environ. 306 (2022) 121111, https://doi.org/10.1016/j.apcatb.2022.121111.

[32] X. Shi, W. Dai, X.A. Dong, Q. Ren, J. Sheng, F. Dong, Dual Cu and S vacancies boost CO_2 photomethanation on $Cu_{1.95}S_{1-x}$: vacancy-regulated selective photocatalysis, Appl. Catal. B Environ. 339 (2023) 123147, https://doi.org/10.1016/j.apcatb.2023.123147.

[33] M. He, W. An, Y. Wang, Y. Men, S. Liu, Hybrid metal–boron diatomic site embedded in C_2N monolayer promotes C–C coupling in CO_2 electroreduction, Small 17 (2021) 2104445, https://doi.org/10.1002/smll.202104445.

[34] Y. Luo, K. Xie, P. Ou, C. Lavallais, T. Peng, Z. Chen, Z. Zhang, N. Wang, X.-Y. Li, I. Grigioni, B. Liu, D. Sinton, J.B. Dunn, E.H. Sargent, Selective electrochemical synthesis of urea from nitrate and CO_2 via relay catalysis on hybrid catalysts, Nat. Catal. 6 (2023) 939–948, https://doi.org/10.1038/s41929-023-01020-4.

[35] S. Zhang, J. Geng, Z. Zhao, M. Jin, W. Li, Y. Ye, K. Li, G. Wang, Y. Zhang, H. Yin, H. Zhang, H. Zhao, High-efficiency electrosynthesis of urea over bacterial cellulose regulated Pd–Cu bimetallic catalyst, EES Catal. 1 (2023) 45–53, https://doi.org/10.1039/D2EY00038E.

[36] M. Qiu, X. Zhu, S. Bo, K. Cheng, N. He, K. Gu, D. Song, C. Chen, X. Wei, D. Wang, Y. Liu, S. Li, X. Tu, Y. Li, Q. Liu, C. Li, S. Wang, Boosting electrocatalytic urea production via promoting asymmetric C–N coupling, CCS Chem. (2023) 1–11, https://doi.org/10.31635/ccschem.023.202202408.

[37] Y. Li, S. Zheng, H. Liu, Q. Xiong, H. Yi, H. Yang, Z. Mei, Q. Zhao, Z.-W. Yin, M. Huang, Y. Lin, W. Lai, S.-X. Dou, F. Pan, S. Li, Sequential co-reduction of nitrate and carbon dioxide enables selective urea electrosynthesis, Nat. Commun. 15 (2024), https://doi.org/10.1038/s41467-023-44131-z.

[38] Y. Zhao, Y. Ding, W. Li, C. Liu, Y. Li, Z. Zhao, Y. Shan, F. Li, L. Sun, F. Li, Efficient urea electrosynthesis from carbon dioxide and nitrate via alternating Cu–W bimetallic C–N coupling sites, Nat. Commun. 14 (2023) 4491, https://doi.org/10.1038/s41467-023-40273-2.

[39] X. Wei, X. Wen, Y. Liu, C. Chen, C. Xie, D. Wang, M. Qiu, N. He, P. Zhou, W. Chen, J. Cheng, H. Lin, J. Jia, X. Fu, S. Wang, Oxygen vacancy-mediated selective C-N coupling toward electrocatalytic urea synthesis, J. Am. Chem. Soc. 144 (2022) 11530–11535, https://doi.org/10.1021/jacs.2c03452.

[40] C. Lv, C. Lee, L. Zhong, H. Liu, J. Liu, L. Yang, C. Yan, W. Yu, H.H. Hng, Z. Qi, L. Song, S. Li, K.P. Loh, Q. Yan, G. Yu, A defect engineered electrocatalyst that

promotes high-efficiency urea synthesis under ambient conditions, ACS Nano 16 (2022) 8213–8222, https://doi.org/10.1021/acsnano.2c01956.

[41] H. Liu, J. Li, J. Arbiol, B. Yang, P. Tang, Catalytic reactivity descriptors of metal-nitrogen-doped carbon catalysts for electrocatalysis, EcoEnergy 1 (2023) 154–185, https://doi.org/10.1002/ece2.12.

[42] Y. Huang, R. Yang, C. Wang, N. Meng, Y. Shi, Y. Yu, B. Zhang, Direct electrosynthesis of urea from carbon dioxide and nitric oxide, ACS Energy Lett. 7 (2021) 284–291, https://doi.org/10.1021/acsenergylett.1c02471.

[43] J. Fu, Y. Yang, J. Hu, Dual-sites tandem catalysts for C–N bond formation via electrocatalytic voupling of CO_2 and nitrogenous small molecules, ACS Mater. Lett. 3 (2021) 1468–1476, https://doi.org/10.1021/acsmaterialslett.1c00375.

[44] S. Zhang, M. Jin, H. Xu, X. Zhang, T. Shi, Y. Ye, Y. Lin, L. Zheng, G. Wang, Y. Zhang, H. Yin, H. Zhang, H. Zhao, An oxygen-coordinated cobalt single-atom electrocatalyst boosting urea and urea peroxide production, Energ. Environ. Sci. (2024), https://doi.org/10.1039/D3EE03399F.

[45] J. Zhou, S. Han, R. Yang, T. Li, W. Li, Y. Wang, Y. Yu, B. Zhang, Linear adsorption enables NO selective electroreduction to hydroxylamine on single Co sites, Angew. Chem. Int. Ed. 62 (2023) e202305184, https://doi.org/10.1002/anie.202305184.

[46] M. Jiang, M. Zhu, M. Wang, Y. He, X. Luo, C. Wu, L. Zhang, Z. Jin, Review on electrocatalytic coreduction of carbon dioxide and nitrogenous species for urea synthesis, ACS Nano 17 (2023) 3209–3224, https://doi.org/10.1021/acsnano.2c11046.

[47] M. Yuan, Q. Li, J. Zhang, J. Wu, T. Zhao, Z. Liu, L. Zhou, H. He, B. Li, G. Zhang, Engineering surface atomic architecture of NiTe nanocrystals toward efficient electrochemical N_2 fixation, Adv. Funct. Mater. 30 (2020) 2004208, https://doi.org/10.1002/adfm.202004208.

[48] M. Sun, G. Wu, J. Jiang, Y. Yang, A. Du, L. Dai, X. Mao, Q. Qin, Carbon-anchored molybdenum oxide nanoclusters as efficient catalysts for the electrosynthesis of ammonia and urea, Angew. Chem. Int. Ed. 62 (2023) e202301957, https://doi.org/10.1002/anie.202301957.

[49] Z. Li, S. Ji, C. Wang, H. Liu, L. Leng, L. Du, J. Gao, M. Qiao, J.H. Horton, Y. Wang, Geometric and electronic engineering of atomically dispersed copper-cobalt diatomic sites for synergistic promotion of bifunctional oxygen electrocatalysis in zinc–air batteries, Adv. Mater. 35 (2023) 2300905, https://doi.org/10.1002/adma.202300905.

[50] J. Zhang, Q. Huang, J. Wang, J. Wang, J. Zhang, Y. Zhao, Supported dual-atom catalysts: preparation, characterization, and potential applications, Chin. J. Catal. 41 (2020) 783–798, https://doi.org/10.1016/S1872-2067(20)63536-7.

[51] Z. Yu, C. Si, A. LaGrow, Z. Tai, W. Caliebe, A. Tayal, M. Sampaio, J.P. Sousa, I. Amorim, A. Araujo, L. Meng, J. Faria, J. Xu, B. Li, L. Liu, Iridium–Iron diatomic active sites for efficient bifunctional oxygen electrocatalysis, ACS Catal. 12 (2022) 9397–9409, https://doi.org/10.1021/acscatal.2c01861.

[52] J. Yi, X. Gao, H. Zhou, W. Chen, Y. Wu, Design of Co-Cu diatomic site catalysts for high-efficiency synergistic CO_2 electroreduction at industrial-level current density, Angew. Chem. Int. Ed. 61 (2022) e202212329, https://doi.org/10.1002/anie.202212329.

[53] H. Funke, A.C. Scheinost, M. Chukalina, Wavelet analysis of extended x-ray absorption fine structure data, Phys. Rev. B 71 (2005) 232, https://doi.org/10.1103/PhysRevB.71.094110.

[54] X. Wei, Y. Liu, X. Zhu, S. Bo, L. Xiao, C. Chen, T. Nga, Y. He, M. Qiu, C. Xie, D. Wang, Q. Liu, F. Dong, C. Dong, X. Fu, S. Wang, Dynamic reconstitution between copper single atoms and clusters for electrocatalytic urea synthesis, Adv. Mater. 35 (2023) 2300020, https://doi.org/10.1002/adma.202300020.